Structural inheritance controlled by olivine viscous anisotropy in fossil mantle shear zones with different past kinematics

Lucan Mameri, Andréa Tommasi, Alain Vauchez, Javier Signorelli, Riad Hassani

Author copy of the article published in Tectonophysics in July 2023. For citations, please refer to the published version:

Mameri, L., Tommasi, A., Signorelli, J., Hassani, R., Vauchez, A. Structural inheritance controlled by olivine anisotropy in fossil mantle shear zones with different past kinematics. Tectonophysics, 863, 229982; 10.1016/j.tecto.2023.229982

Structural inheritance controlled by olivine viscous anisotropy in fossil mantle shear zones with different past kinematics

Lucan Mameri [a,1,*], Andréa Tommasi [a,*], Alain Vauchez [a], Javier Signorelli [b], Riad Hassani [c]

[a] Géosciences Montpellier, CNRS & Université de Montpellier, France
[b] Instituto de Física de Rosario, CONICET & Universidad Nacional de Rosario, Argentina
[c] Géoazur, Observatoire de la Côte d'Azur, CNRS & Université Côte d'Azur, IRD, France

Keywords:
Olivine CPO
Viscous anisotropy
Lithospheric shear zone
Strain localization
Structural reactivation
Structural inheritance
Numerical modeling

A B S T R A C T

Geophysical and geological observations hint for the presence in the lithospheric mantle of both active and fossil shear zones with varied past kinematics. Shear in the lithospheric mantle produces olivine crystallographic preferred orientations (CPO), which lead to dependence of the viscous behavior on the direction of the load. Yet, the role of anisotropic viscosity in the mantle is seldom considered in models of structural reactivation. Here, we present 3-D geodynamic finite-element models that quantify the strain and viscosity distribution in a lithosphere containing a fossil thrust (or extensional) mantle shear zone with variable orientation relatively to a new extensional or compressional tectonics. The results were compared to that of a fossil strike-slip mantle shear zone. The fossil olivine CPO in the shear zone produces an anisotropic response of the lithospheric mantle, which is modelled using a parameterized description of viscous anisotropy derived from polycrystal plasticity simulations. We found that CPO-induced reactivation of fossil extensional or thrust mantle shear zones is favored for dips 30–60°, with maximum strain localization if the load is normal to the trend of a fossil shear zone dipping by 45°-50°. This represents a broader range of reactivation potential than in fossil strike-slip mantle shear zones. Both fossil shear zones trending at 45° to the imposed load are reactivated regardless of their dip. For a given viscous anisotropy in the lithospheric mantle (i.e., fossil shear zone orientation), the associated strain localization in the crust is always higher under extensional reactivation, where strain rates may be up to ~100 times higher than those in the (isotropic) surrounding crust. These results imply that viscous anisotropy associated with fossil mantle shear zones plays a key role in large-scale structural reactivation during successive tectonic episodes, shaping the current lithospheric architecture, such as in the Pyrenees and Norwegian margin.

1. Introduction

It has long been noticed that major lithospheric structures formed in rifts and orogens are often reactivated during subsequent tectonic events (Wilson, 1966). This observation is corroborated by the parallelism between ancient lithospheric-scale shear zones and present-day geological and geophysical structures within continents (cf. examples in Tommasi and Vauchez, 2001; Vauchez et al. 1997, Vissers and Meijer, 2012). Seismic anisotropy associated with these shear zones, in particular splitting of teleseismic shear (*S*)-waves, results mainly from strain-induced crystal preferred orientations (CPO) of olivine in the upper ~200 km of the mantle (Nicolas and Christensen, 1987). Hence, coherent patterns of teleseismic S-wave splitting data over domains tens to hundreds of km-wide within continents (splitting.gm.univ-montp2.fr/DB) are interpreted as due, at least in part, to olivine CPO formed during deformation in major past tectonic episodes and now fossilized in the lithospheric mantle.

High delay times (>1 s) of teleseismic S-wave splitting and fast polarization directions sub-parallel to the trend of lithospheric-scale shear zones with strike-slip, transtensive or transpressive kinematics, together with high Pn anisotropy suggest that such shear zones crosscut the entire lithosphere (Judenherc et al., 1999; Vauchez and Tommasi, 2003; *review in* Vauchez et al., 2012). This pattern is particularly clear along active continental transform plate boundaries, like the Alpine (Duclos et al., 2005) and San Andreas faults (Hartog and Schwartz, 2001; Bonnin et al., 2012). It is also observed along large intraplate transcurrent or

* Corresponding authors.
E-mail addresses: lucanmameri@gmail.com (L. Mameri), andrea.tommasi@umontpellier.fr (A. Tommasi).
[1] Present address: Department of Earth and Atmospheric Science, The City College of New York, NY, USA.

transpressive shear zones of various ages, like the Kunlun fault in the Himalayas (Hirn et al., 1995) or the Grenville front in Canada (Sénéchal et al., 1996).

Usually, shallowly- to moderately dipping extensional or compressional shear zones do not generate clear teleseismic S-wave splitting, likely due to the limited thickness sampled by the wave path. However, in some cases, the presence of such shear zones in the lithospheric mantle may be inferred from the observation of fast polarization direction of S-wave sub-perpendicular to the shear zone trend, as in the Mid-Norway margin (Grund and Ritter, 2020) or the Moine Thrust in the Scottish Highlands (Bastow et al., 2007). Extensional shear zones in the lithospheric mantle are more commonly inferred based on deep seismic reflectors, as those observed beneath the Basin and Range (Catchings and Mooney, 1991) and the Norwegian margin (Peron-Pinvidic and Osmundsen, 2020). Another robust line of evidence for the existence of extensional shear zones crosscutting the lithospheric mantle comes from exhumed peridotite massifs, as Lanzo (Kaczmarek and Tommasi, 2011), Beni Bousera (Frets et al., 2014), and Erro-Tobio (Vissers et al., 1995), which display km-scale mantle shear zones accommodating lithospheric thinning. Thrust shear zones in the mantle are more rarely exposed, but they have been mapped in the field in the Oman ophiolite (e.g., Boudier and Coleman, 1981) and inferred from deep seismic transects across the Pyrenees (Muñoz, 1992) and the Alps (Nicolas et al., 1990).

Olivine CPO produces not only anisotropy of the elastic behavior (e.g., anisotropy of seismic waves propagation), but also of the viscous behavior, as indicated by direct experimental measurements in hot-pressed (Hansen et al., 2012) and natural (Meyers and Kohlstedt, 2021) olivine aggregates. Viscous anisotropy associated with coherent olivine CPO at plate-scale has been argued to result in lateral variations in strength of the lithospheric mantle (Tommasi and Vauchez, 2001, 2015). Numerical models coupling polycrystal plasticity and geodynamic simulations predict that CPO-induced viscous anisotropy in the lithospheric mantle may lead to reactivation of fossil vertical strike-slip shear zones if the new tectonic load is oblique to the shear zone trend (Knoll et al., 2009; Tommasi et al., 2009). More recent geodynamic simulations, in which olivine-induced viscous anisotropy is implemented via a parameterization derived from polycrystal plasticity simulations, showed that viscous anisotropy associated with fossil vertical strike-slip shear zones in the mantle may trigger strain localization with strong along-strike component in both the mantle and overlying crust (Mameri et al., 2021). The orientation of the olivine CPO in a mantle shear zone, and the resulting anisotropic response, depends on the shear zone kinematics (Tommasi et al., 1999). Extensional or thrust mantle shear zones exhibit stretching lineations and, in most cases, olivine CPO characterized by [100]-maxima at high angle to the shear zone trend, whereas strike-slip shear zones exhibit both stretching lineations and olivine CPO characterized by [100]-maxima parallel to their trend. Therefore, the loading geometries in which CPO-induced viscous anisotropy in the lithospheric mantle will produce reactivation of the fossil structures will probably differ as a function of the shear zone's past kinematics.

The role of CPO-induced viscous anisotropy in fossil mantle shear zones has often been overlooked in models of large-scale structural reactivation and tectonic inversion, which tend to focus on structural inheritance in the crust (e.g., Jackson, 1980; Butler, 1989). Reactivation of Variscan lithospheric-scale shear zones, which affected both the crust and the lithospheric mantle, was, nevertheless, proposed to play an important role in both the Pyrenean rifting and orogeny (Vauchez et al., 1997; Saspiturry et al., 2020). Reactivation of Caledonian lithospheric-scale shear zones was also proposed as an important factor in the early-phase of stretching in the hyperextended Norwegian margin (Peron-Pinvidic and Osmundsen, 2020). In the present study, we explore the role of anisotropic viscosity of mantle structures with different past kinematics on large-scale structural reactivation in a quantitative manner, addressing the following questions: Does CPO-induced viscous anisotropy in fossil extensional or thrust mantle shear zones favor strain localization? If yes, for which orientations of the tectonic load relative to the fossil mantle structures? What is the magnitude of strain localization compared to that associated with reactivation of fossil strike-slip mantle shear zones? Does strain localization propagate from the mantle to the crust? If so, how do gravity forces affect the reactivation and impact lithospheric thickness?

2. Methods

2.1. Modeling CPO-induced viscous anisotropy

To model the effect of the viscous anisotropy of olivine CPO on plate-scale deformation we build on our previous work (Mameri et al., 2019), in which the viscoplastic anisotropy of olivine aggregates was modelled using the second-order viscoplastic self-consistent approach (SO-VPSC; Ponte Castañeda, 2002). This approach considers average intragranular fluctuations in strain-rate and stress, which makes it a good choice for approximating the effective behavior of polycrystals composed of highly anisotropic crystals such as olivine. The SO-VPSC simulations are used to parameterize the CPO-induced viscoplastic anisotropy of an olivine polycrystal using the Hill (1948) yield function (Signorelli et al., 2021). The viscous anisotropy associated with a given olivine CPO is described by six material coefficients (F,G,H,L,M,N) obtained in the CPO reference frame (Table 1). The coefficients are calibrated using olivine polycrystals composed of 1000 grains and slip systems data (Table 2) derived from high-temperature, moderate pressure laboratory experiments of deformed olivine single crystals (Bai et al., 1991). Since only dislocation creep is considered, the calculations provide an upper bound for viscous anisotropy of olivine at lithospheric conditions (Mameri et al., 2019). The anisotropy coefficients depend mainly on the olivine CPO symmetry and intensity. This parameterization was implemented in the elasto-visco-plastic thermomechanical code Adeli3D, which is based on a Lagrangian finite-element discretization (Hassani et al., 1997). For details on the parameterization of the viscous anisotropy of olivine polycrystals and its implementation in the geodynamical code refer to Signorelli et al. (2021).

Here, this geodynamic code is employed to model a lithosphere containing a viscous anisotropic mantle with thermally-activated non-linear rheology, simulating deformation by dislocation creep. Shortening or stretching is imposed on a continental lithosphere containing a fossil mantle shear zone with varied past kinematics trending normal to the imposed tectonic load. The aim is to evaluate the reactivation potential of fossil extensional (or thrust) mantle shear zones with variable dip angles and to compare this reactivation potential with that of fossil strike-slip mantle shear zones.

To obtain first-order predictions of the effect of viscous anisotropy on the mantle shear zones strength, we first computed using the SO-VPSC model the instantaneous anisotropic response of an olivine polycrystal with a strong orthorhombic CPO for a large range of loading-geometries (Fig. 1). These SO-VPSC simulations consider an olivine CPO with the same symmetry, intensity (J = 12.7), number of grains (n = 1000) and

Table 1
Hill coefficients for random, weak, intermediate and strong orthorhombic olivine CPO.

Coefficients	F	G	H	L	M	N
Isotropic (J = 1)	0.50	0.50	0.50	1.50	1.50	1.50
Anisotropic* (J = 2.8)	0.19	0.37	0.51	2.85	1.59	1.67
Anisotropic* (J = 6.8)	0.06	0.31	0.45	5.24	1.73	1.88
Anisotropic* (J = 12.7)	0.02	0.22	0.37	8.91	2.12	2.30

* CPO with [100]- and [010]-maxima parallel to X and Y of the pole figure, respectively. J-index (J)

Table 2
Slip systems parameters used in the SO-VPSC simulations.

Slip systems	Critical resolved shear stress #	Stress exponent
(010)[100]	1	3
(001)[100]	1	3
(010)[001]	2	3
(100)[001]	3	3
(011)[100]	4	3
(110)[001]	6	3
{111}⟨110⟩[a]	50	3
{111}⟨011⟩[a]	50	3
{111}⟨101⟩[a]	50	3

[#] Adimensional values, normalized by the flow stress of the (010)[100] slip system, derived from high temperature, moderate pressure experiments on olivine single crystals (Bai et al., 1991).

[a] Slip systems not active in olivine, used for stabilizing the calculations; they accommodate <5% strain in all simulations.

relative slip systems strength (see CRSS in Table 2) than those used to estimate the viscous anisotropy parameters of most geodynamical simulations in this study. Axial shortening was imposed at 15° intervals relative to the maximum concentration of the [100] axes of the olivine CPO. The estimated mechanical response (stress required to accommodate the imposed shortening) was normalized to that of an isotropic polycrystal. These simulations provide a first hint on the reactivation potential of fossil mantle shear zones with strike-slip (Fig. 1a) or extensional (or thrust; Fig. 1b) past kinematics as a function of their trend (θ°) and dip (α°) relative to a horizontal tectonic load. To mimic the boundary conditions in the geodynamical models, mixed boundary conditions were imposed to the SO-VPSC simulations, that is, a constant velocity was applied along the direction Y and equal non-null constant stresses were applied along the directions X and Z; shear velocities were null (see §2.3.2 in Signorelli et al., 2021 *for details*). In these polycrystal plasticity simulations, shortening and extension are equivalent, since olivine does not develop mechanical twinning.

The SO-VPSC simulations predict that the lowest strength produced by olivine viscous anisotropy should be observed in (1) fossil vertical strike-slip shear zones trending at 45° to the imposed shortening (case #1 in Fig. 1a) or stretching, and (2) in fossil extensional (or thrust) mantle shear zones dipping by 45° trending normal to the imposed shortening or stretching (case #2/3 in Fig. 1b). These simulations also imply that fossil mantle shear zones trending at 45° to the imposed tectonic load are always favorably oriented to be reactivated, independently of their dip (red and black circles in Figs. 1a, b indicate a lower strength than that of an isotropic olivine polycrystal). In the following geodynamical models, we examine the reactivation potential of fossil strike-slip and extensional (or thrust) mantle shear zones oriented perpendicular to the tectonic load with varied dip angles, and compare it to the reactivation potential of vertical strike-slip mantle shear zones trending at various angles to the tectonic load. The SO-VPSC simulations predicts sharp contrast in mechanical behavior in these orientation-relations (see circles enclosed by dashed lines in Figs. 1a, b), indicating potential reactivation only when the shear plane is at ~45° to the load.

2.2. Geodynamical model setup

The models simulate a continental lithosphere 1100 km-long, 500 km-wide and 120 km-deep, consisting of a 40 km-thick crust and an 80 km-thick lithospheric mantle (Fig. 2). The asthenosphere was not considered. The crust is homogenous and isotropic in all runs. The mantle comprises a 50 km-wide tabular zone representing a fossil shear zone. In most runs, this zone is characterized by an orthorhombic olivine CPO consistent with simple shear deformation (Tommasi et al., 1999), with a strong CPO intensity (J-index = 12.7, M-index = 0.42), while the surrounding mantle has a random olivine CPO (J-index = 1, M-index = 0). We also tested intermediate (J-index = 6.2, M-index = 0.25) and weak CPO intensities (J-index of 2.8, M-index = 0.12) within the mantle shear zone, as well as a strong olivine CPO in the surrounding mantle with an orientation different from that of the mantle shear zone. The tested CPO intensities sample the range observed in naturally deformed mantle peridotites (Tommasi and Vauchez, 2015). In all simulations the bulk shortening or stretching remained <10%, allowing us to neglect the

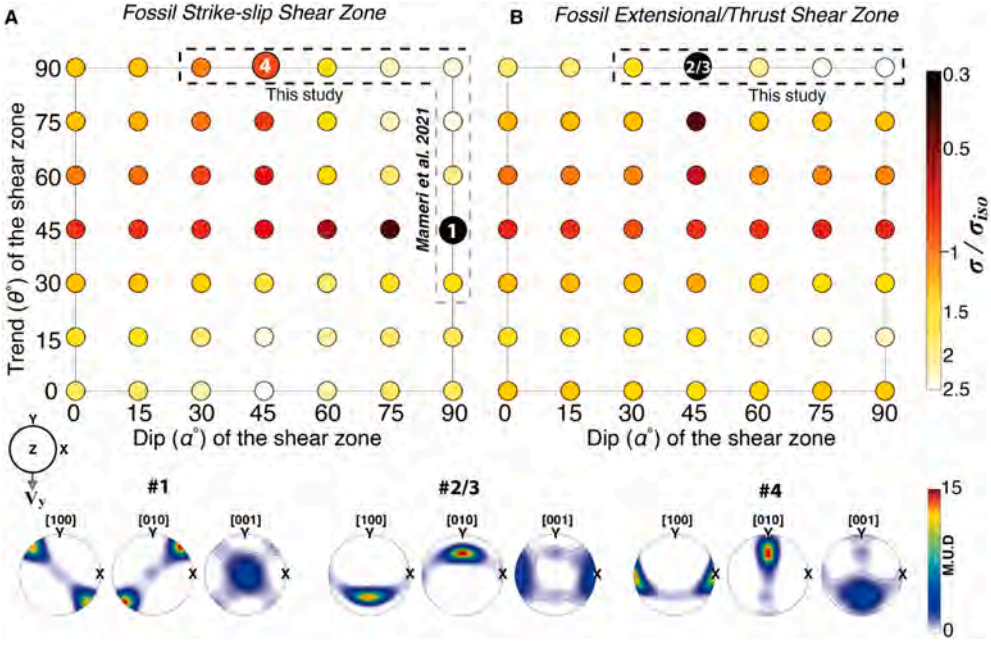

Fig. 1. Strength of an olivine polycrystal with a strong orthorhombic CPO (J = 12.7) subjected to axial extension (Vy) at different angles to the CPO (cf. reference frame in insert at the top left of pole figures) relative to the isotropic polycrystal; calculated using the second-order viscoplastic self-consistent (SO-VPSC) approach. The CPO is oriented as expected in fossil a) strike-slip (horizontal [100]-maximum) and b) extensional/thrust (down-dip [100]-maximum) mantle shear zones with different orientations of strike and dip relative to a horizontal tectonic load. Black-red circles characterize anisotropic polycrystals weaker than the isotropic polycrystal (ratio between bulk Von Mises equivalent stresses), whereas yellow-white circles characterize anisotropic polycrystals stronger than the isotropic (J = 1) one. The dashed domains indicate the orientation-relations studied by geodynamic modeling, while the numbers inside the circles correspond to the simulations presented in detail in Figs. 3-5. The orientation-relation between the extension direction and the olivine CPO for the four numbered simulations are displayed as pole figures. (M.U.D: Multiples of Uniform Distribution).

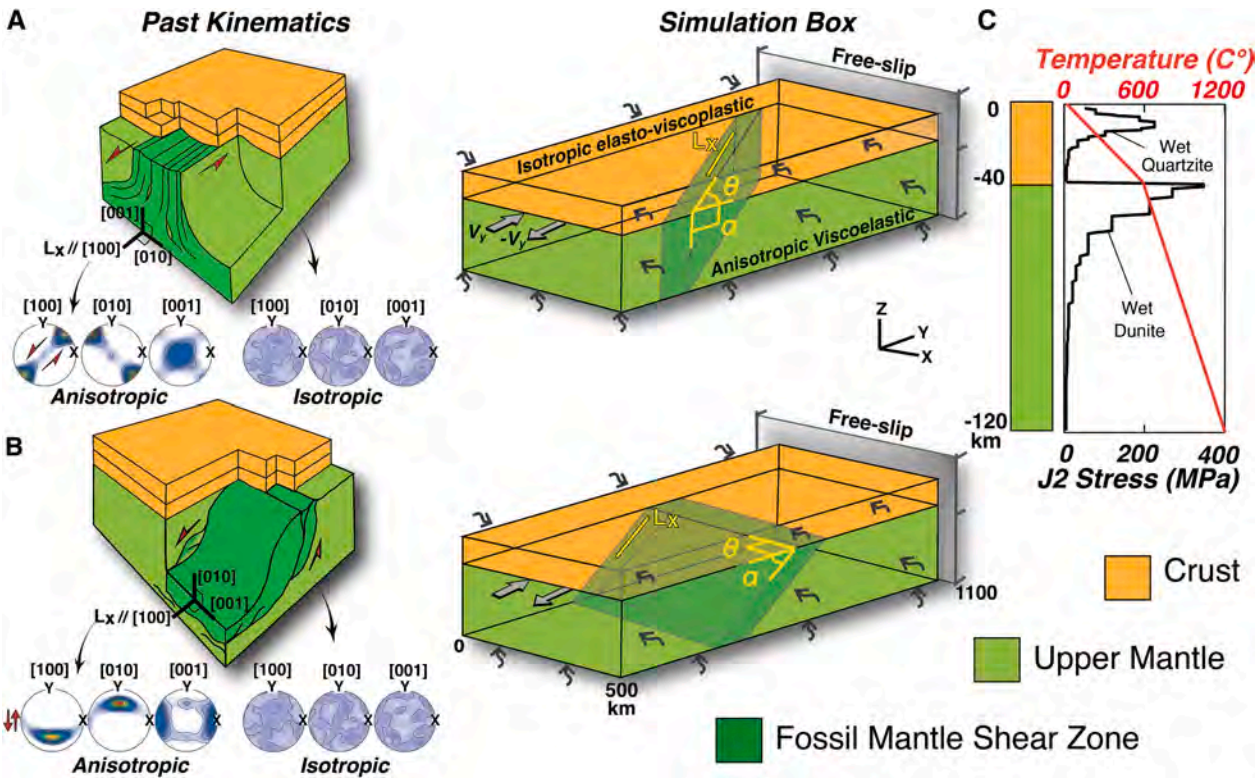

Fig. 2. Geometry and boundary conditions of the geodynamical simulations. The simulation box represents a continental plate containing: A) a fossil strike-slip shear zone that, as in Mameri et al., 2021, the dip angle (α) is constant, vertical, with trend (θ) at variable orientations to the imposed horizontal compression (V_y) or extension ($-V_y$) (shown above, α=90, θ=45°), or, as in the present study, dip α vary while the trend is constant at θ=90°; B) a fossil extensional or thrust shear zone with variable dip trending normal to the load direction (shown above, α=45°, θ=90°). The anisotropic fossil shear zone is solely defined by a change in the orientation or intensity of the olivine CPO in the mantle. As represented in the left panel, the [100]-maximum of the olivine CPO follows the stretching lineation (Lx); it is horizontal, along-trend in fossil strike-slip mantle shear zones, and it is down-dip, normal-trend in fossil extensional (or thrust) mantle shear zones. In most runs, the mantle surrounding the shear zone has a random CPO. C) Geotherm and predicted differential stress profile for a constant strain rate of $\sim 10^{-15}$ s^{-1}. Wavy-arrows in the bottom and lateral planes of the simulation boxes represent lithostatic pressure boundary conditions; see text (§2.2) for details.

evolution of the olivine CPO in response to the imposed load.

In this study, we simulated fossil mantle shear zones trending normal to an imposed shortening or stretching ($\theta = 90°$), but with variable dip angles ($\alpha = 30° - 90°$). In most cases, the fossil mantle stretching lineation (L_x) and, hence, the maximum concentration of [100]-axes of the olivine CPO within the mantle shear zone plunges down-dip, simulating past extensional or thrust kinematics (Fig. 2b); from now on called 'fossil extensional/thrust mantle shear zone'. We also ran a few models with a mantle shear plane with variable dip angles and [100]-maximum parallel to the shear zone trend in a horizontal orientation, simulating shallow to moderate dipping mantle shear zones with past strike-slip kinematics. The results are compared with the response of a fossil strike-slip mantle shear zone with a vertical shear plane trending between 30° and 90° to the tectonic load (Fig. 2a). Independently of the dip of the mantle shear plane, fossil shear zones with horizontal stretching lineation, and thus [100]-maximum, are referred to as 'strike-slip' in this study, and we distinguish them by the dip of the shear plane: vertical (as in Mameri et al., 2021) or moderately dipping (this study). The reactivation potential of fossil mantle shear zones oriented at low angles (<30°) to the imposed load direction is inferred utilizing SOVPSC simulations and the symmetry between complementary angles (e.g., 90° with 0° and 75° with 15°) in the strain localization pattern as the trend or dip of the shear plane vary. This approach was employed because such low angles of strike or dip requires very large simulation boxes to prevent the tabular shear zone from intersecting the boundary where the velocity is imposed. A summary of the geodynamical models explored in this study is presented in the supplementary material (Table S1).

Tectonic load was enforced by imposing a constant horizontal velocity ($V_y = 3$ cm/y) normal to the left lateral boundary of the simulation box and free-slip conditions ($V_y = 0$) at the opposed lateral boundary. Lithostatic pressure conditions were ascribed to the other lateral and the bottom boundaries. The upper boundary was set free. Gravitational forces were considered. Linear geothermal gradients were specified in the crust and mantle, with constant temperatures of 25 °C and 1200 °C at the top and bottom boundaries of the simulation box, respectively, and Moho temperature of 600 °C (Fig. 2c). A constant density (ρ) of 3000 kg/m^3 was assigned to both mantle and crust. This value represents the average density for a crust with $\rho = 2600$ kg/m^3 and a mantle with $\rho = 3300$ kg/m^3, weighted for thicknesses of 80 km and 40 km, respectively. The crust was discretized by 5 km-wide tetrahedral mesh-elements and the mantle by 10 km-wide tetrahedral mesh-elements. In a few cases, the mesh in the crust atop the intersection between the fossil mantle shear zone and the Moho was refined by a factor 2 (supplementary Fig. S4).

Brittle deformation in the upper crust was modelled by an elasto-plastic rheology that follows an isotropic pressure-dependent Drucker-Prager yield criterion, with a cohesive strength of 10 MPa. Frictional weakening was imposed by decreasing the internal angle of friction from 30° to 15° at 1% of plastic strain in the mesh-element. The ductile deformation in the crust was modelled using a thermally-activated isotropic viscous rheology with a wet quartzite dislocation creep flow law (Paterson and Luan, 1990). This rheology results in maximum stresses of ~250 MPa at a strain rate of $\sim 10^{-15}$ s^{-1}. The ductile deformation in the mantle was modelled using a thermally-activated viscous rheology with a wet dunite dislocation creep flow law (Chopra and

Paterson, 1981), modified to account for the parametrized CPO-induced viscous anisotropy (Signorelli et al., 2021). By utilizing this flow law, we do not imply that the lithospheric mantle is wet. Rather, this flow law is employed because it produces maximum stresses of ~400 MPa in the shallowest mantle at a strain rate of $\sim 10^{-15}$ s^{-1}, consistent with predictions of recent flow laws for dry olivine accounting for the power law breakdown (Gouriet et al., 2019). Isotropic material parameters are summarized in Table 3.

3. Results

Strain localization was quantified by the ratio between the average strain rate, defined as the average of the 2nd invariant of the strain rate tensor $J_2(D)$, in the fossil mantle shear zone and in the crustal domain located in the upward continuation of the mantle shear zone, and the average strain rate in the surrounding mantle and crust, respectively. Strain localizes in fossil strike-slip and extensional/thrust mantle shear zones when both [100]- and [010]-maxima of the olivine CPO are oblique to the imposed load direction (Fig. 3b). A strain localization factor of ~30 is observed in a fossil extensional/thrust mantle shear zone dipping by 45° and trending normal to the imposed extension (case #2, $\theta = 90°, \alpha = 45°$). This strain localization factor is very close to that (~28) displayed by a vertical fossil strike-slip mantle shear zone trending at 45° to the imposed compression (case #1, $\theta = 45°, \alpha = 90°$; Mameri et al., 2021) or extension. Reactivation of a fossil extensional/thrust mantle shear zone dipping by 45° and trending normal to the imposed extension results, however, in a much higher strain localization factor in the overlying crust (~100; see case #2 in Fig. 3a) than that in the crust above a reactivated fossil vertical strike-slip mantle shear zones trending at 45° to the imposed load (factor ~9; see case #1 in Fig. 3a).

If the deformation is compressional, instead of extensional, the strain localization associated with fossil extensional/thrust mantle shear zones is significantly reduced. In compression, the maximum strain localization factor associated with reactivated fossil extensional/thrust mantle shear zones is ~4, observed within fossil mantle shear zones dipping by 45° and trending normal to the load direction. This is ~7 times smaller than the maximum strain localization factor within the same fossil structure subjected to extension (compare cases #2 and #3 in Fig. 3). The contrast in behavior between extension and compression is even more marked in the crust (Fig. 3a), where maximum strain localization factor is ~4 in compression and ~100 in extension.

For vertical fossil strike-slip mantle shear zones trending at 45° to the imposed tectonic load, the models predict similar strain localization factors in extension and compression (supplementary Fig. S1). However, in the first case, the shear zone is reactivated in transtension and in the second, in transpression. For angles <45° between the fossil shear zone trend and the imposed load direction, the strain localization factor is slightly higher in compression than in extension; the opposite is observed for angles >45°. As for fossil extensional/thrust mantle shear zones, the crustal response is more sensitive to the imposed deformation

Table 3
Isotropic material parameters used in the geodynamical simulations.

	Wet quartzite[a]	Wet dunite[b]
Density (kg m^{-3}) ρ	3000	3000
Young modulus (GPa)	70	160
Poisson ratio	0.25	0.28
Fluidity ($Pa^{-n} s^{-1}$) γ_0	1.63×10^{-26}	3.98×10^{-25}
Activation Energy (kJ $mol^{-1} K^{-1}$) Q	135	498
Stress exponent n	3.1	4.5
Angle of friction* ϕ	30° → 15°	–
Cohesion (MPa) c	10	–

References: [a]Paterson and Luan (1990), [b]Chopra and Paterson (1984)
* Frictional weakening: ϕ is reduced to 15° when plastic strain in the mesh element exceeds 1%.

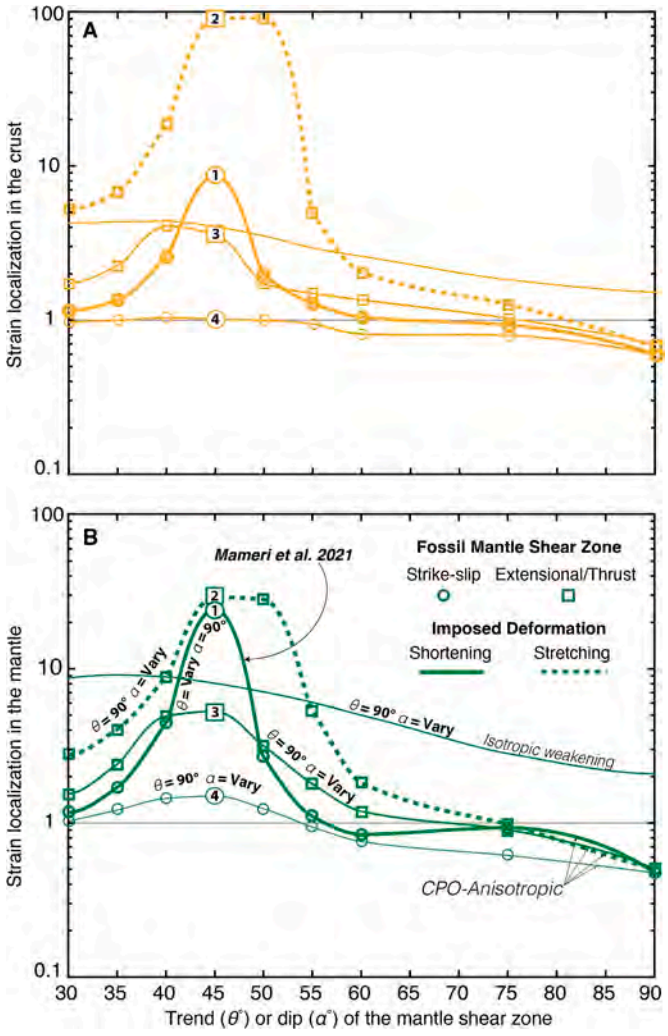

Fig. 3. Strain localization in the (a) crust and in the (b) mantle as a function of the trend (θ) or dip (α) of the fossil mantle shear zone, as indicated on the curves, relative to the direction of the imposed horizontal shortening (continuous lines) or stretching (dashed lines). Values >1 indicate strain localization within the fossil mantle shear zone or within the crust atop it. Circles indicate strike-slip and squares extensional (or thrust) past kinematics. Results are displayed after ~2 m.y. of plate deformation. All simulations have a strong olivine CPO intensity (J = 12.7) in the fossil mantle shear zone and random CPO (J = 1) in the surrounding mantle.

regime: strain localization in the crust atop a fossil vertical strike-slip mantle shear zone trending between 45° and 50° to the imposed load is a factor ~3 higher in extension than in compression. Shallow to moderate dipping fossil strike-slip mantle shear zones trending normal to the load (case #4 in Fig. 3b) are much less prone to be reactivated than the other mantle structures tested. Such fossil mantle shear zones have a higher strength than the surrounding isotropic mantle for dips ≤30° or ≥ 55°. The maximum strain localization factor in the mantle is ~2, which occur in fossil strike-slip mantle shear zones with dip angles of ~40°–45°, and do not result in strain localization in the crust. Strain localization in such fossil structures is slightly higher under extension, but marginally (supplementary Fig. S2).

Reactivation of fossil extensional/thrust mantle shear zones occurs for a larger range of loading-geometries than reactivation of fossil strike-slip mantle shear zones (compare lines passing through cases #1, 2 and 3 in Fig. 3). Fossil extensional/thrust mantle shear zones trending normal to the load direction are reactivated for dip angles varying from 30° to 60°, whereas fossil vertical strike-slip mantle shear zones are only

reactivated when trending from 40° to 50° to the load direction. Higher strength than the surrounding isotropic mantle is predicted for fossil extensional/thrust mantle shear zones dipping from 75° to 90°, and for fossil vertical strike-slip mantle shear zones trending from 60° to 90°. The analysis of Fig. 3 hints at possible, but small, CPO-induced reactivation of shallowly dipping (<30°) fossil extensional/thrust mantle shear zones. In the modelled range of dip angles (30° to 90°), the pattern of strain localization as a function of the dip angle is asymmetric between complementary angles: strain localization in fossil extensional/thrust shear zones dipping by 30° is easier than in those dipping by 60°. This asymmetry in the reactivation potential relative to the dip angle is corroborated by the SO-VPSC simulations (Fig. 1b). However, the VPSC simulations suggest a narrower range of dip angles with potential for reactivation of fossil extensional/thrust shear zones than the geodynamic models. The difference in predictions between the VPSC and geodynamic models results from the greater degree of freedom for deformation of the anisotropic domain in the geodynamical simulations, where the boundary conditions are imposed far from the anisotropic domain. In contrast, in the VPSC simulations, the boundary conditions are imposed directly on the anisotropic domain.

For comparison, we also tested the reactivation potential of a fossil mantle structure characterized by isotropic viscous weakening (100-fold increase in fluidity) with varied dip angle and trending normal to a compressional load (results labelled 'isotropic weakening' in Fig. 3b). As expected, the reactivation potential of an isotropic fossil mantle structure depends less on the orientation of the shear zone than that of an anisotropic one. Isotropic fossil structures are always reactivated, independently of their dip. Under stretching, the strain localization factors associated with such isotropic structures are up to ~3 and ~25 times lower than the maximum ones in the fossil anisotropic structures with strong olivine CPO and crust above it, respectively. But for dips lower than 40° or higher than 50°, they are higher than those of anisotropic fossil mantle structures by <7 times. Under shortening, strain localization factors associated with anisotropic structures with fossil extensional/thrust kinematics (case #3 in Fig. 3) are always lower than those associated with an isotropic planar weakness, in both the mantle and crust.

Analysis of the 2nd invariant of the strain-rate field for fossil mantle shear zones with different past kinematic, in the orientations most prone to be reactivated, highlights further differences on the strain distribution in the lithosphere. Crustal strain localization develops right above the upward continuation of the vertical fossil strike-slip mantle shear zone (case #1), whereas atop fossil extensional/thrust mantle shear zone, it follows the inclined projection of the mantle structure to the crust (case #2). Reactivation associated with fossil vertical strike-slip mantle shear zones trending by 45° to the load direction results in much stronger strain localization in the mantle than in the upper domain of the crust (case #1 in Fig. 4). In contrast, reactivation of fossil extensional/thrust mantle shear zone dipping by 45° and trending normal to the load direction results in more homogenous vertical distribution of strain localization. However, the distribution differs between extension and compression. In extension, strain localization is stronger in the crust than in the mantle (case #2 in Fig. 4), whereas in compression, strain localization is stronger in the mantle (case #3 in Fig. 4). In the lower domain of the crust, high strain rates usually affect a wider domain than the fossil mantle shear zone. As anticipated, deformation is fairly homogenously distributed across the plate If viscous anisotropy does not result in significant strain localization in the mantle, as in strike-slip mantle shear zones normal to the load direction and dipping by 45° (case #4 in Fig. 4).

The contrast in viscous strength between the reactivated mantle shear zone or the newly developed crustal shear zone atop it relative to their isotropic surroundings was also quantified (Fig. 5). We analyzed variations in effective viscosity along horizontal profiles at the center of the simulation box (parallel to y-direction; at x = 250 km), in the uppermost mantle at 52 km depth and in the middle domain of the crust at 18 km depth. CPO-induced strain localization in fossil extensional/thrust mantle shear zones dipping by 45° reactivated in extension normal to their trend produces a contrast in effective viscosity of a factor ~100 in the mantle (case #2 in Fig. 5). In this case, the down-dip displacement along the structure juxtaposes laterally domains with different strengths, resulting in an asymmetric effective viscosity profile in the crust: the lateral viscosity contrast is a factor ~300 across the footwall and a factor ~100 across the hanging wall of the crustal shear zone. If the surrounding mantle has a strong olivine CPO oriented with the maximum concentration of [100]- or [010]-axes respectively parallel and vertically normal to the imposed tectonic load, effective viscosity constrast is significanlty stronger (supplementary Fig. S3).

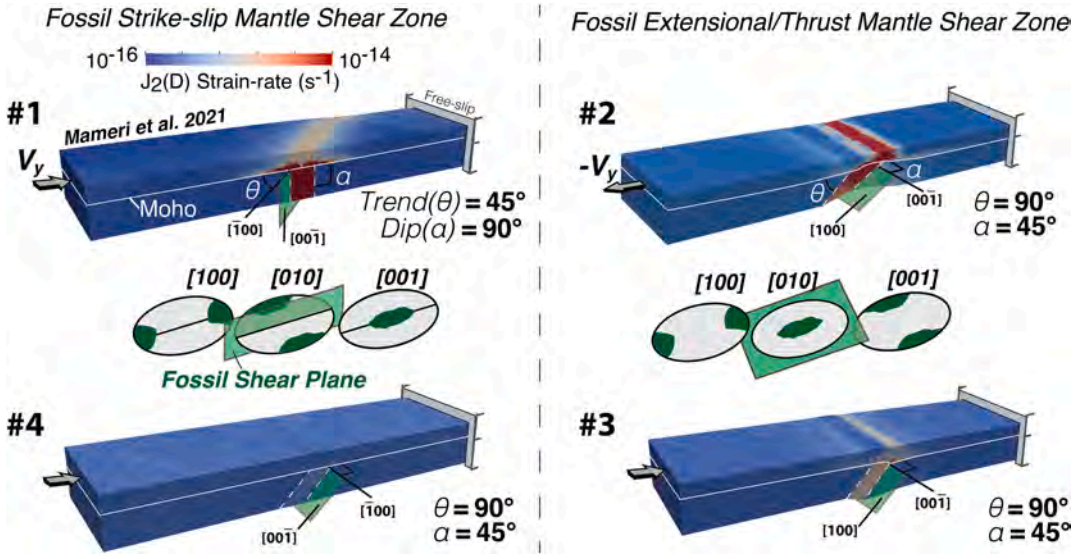

Fig. 4. Strain rate field (2nd invariant of the strain rate tensor) after ~2 m.y. of deformation of a plate containing a fossil strike-slip mantle shear zone (cases #1 and #4) or a fossil extensional/thrust mantle shear zone (cases #2 and #3) in the loading-geometry that produces the most effective reactivation (cf. Fig. 3). The orientation of the olivine CPO and the trend (θ) and dip (α) of the fossil mantle shear plane (in green) with respect to the direction of the imposed load are shown for each case. All simulations have strong olivine CPO intensity (J = 12.7) in the fossil mantle shear plane and random CPO (J = 1) in the surrounding mantle.

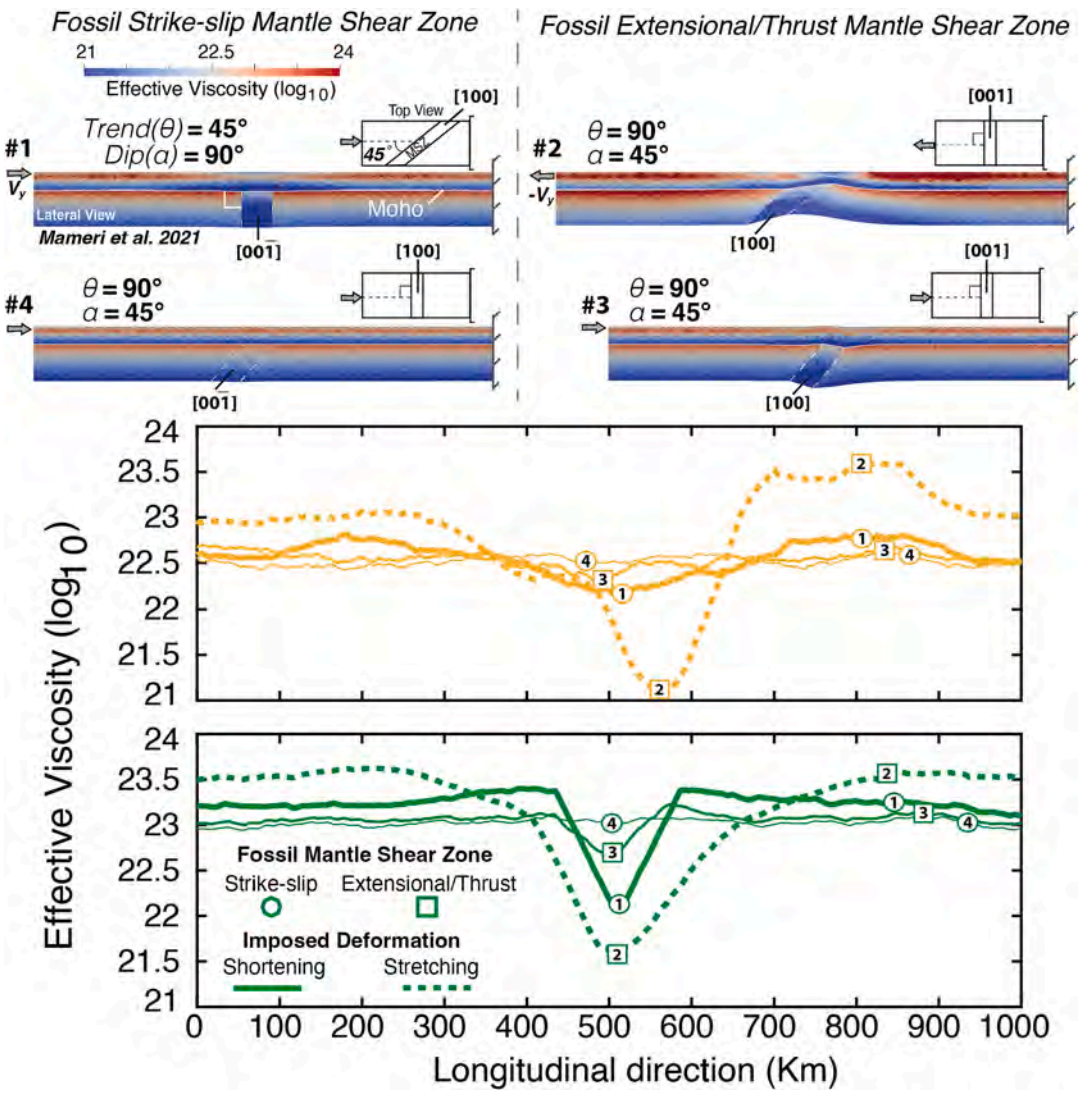

Fig. 5. Effective viscosity fields in the crust (yellow) and mantle (green) after ~2 m.y. of deformation. Top panel: Cross-sections parallel to the imposed shortening or stretching at the centre of the simulation box. Bottom panel: Horizontal profiles at 18 km and 52 km depth along the cross-sections shown in the top panel. Simulations are labelled as in Figs. 3 and 4. The markers in the profiles indicate the past kinematics of the fossil mantle shear zone (circle: strike-slip; square: extensional/thrust) and the type of lines the imposed deformation (continuous: shortening; dashed: stretching). The orientation of the olivine CPO with respect the trend (θ) and dip (α) of the fossil mantle shear plane, and this latter with respect to the direction of the imposed load, are shown in the top panel. All simulations have strong olivine CPO intensity (J = 12.7) in the fossil mantle shear plane and random CPO (J = 1) in the surrounding mantle.

Reactivation of a fossil extensional/thrust mantle shear zone in compression produces a much lower lateral contrasts in effective viscosity: a factor ~3 in the mantle and a factor ~2 in the crust, with no asymmetry in the viscosity profile (case #3 in Fig. 5). Reactivation of a fossil vertical strike-slip mantle shear zone trending by 45° to the imposed shortening (case #1 in Fig. 5) results in an intermediate behavior in terms of its magnitude, with lateral contrasts in effective viscosity by a factor ~20 in the mantle and ~10 in the crust.

Fig. 6 shows the evolution over time of the average vertical strain in the crust and mantle associated with the reactivation of 45° dipping fossil extensional/thrust mantle shear zones trending normal to the imposed extension or compression (down-dip 'dd' cases #2 and #3, respectively), with either weak, intermediate, or strong olivine CPO intensity. These results are compared to that of: *i)* a fossil strike-slip mantle shear zone trending normal to the load direction and dipping by 45° with a strong olivine CPO (strike-slip 'ss' case #4); *ii)* a lithosphere with homogenous and isotropic mantle and crust, that is, absence of a fossil shear zone and olivine CPO ('Isotropic No SZ'); *iii)* a fossil isotropic mantle shear zone trending normal to the load and dipping by 45° characterized by a lower effective viscosity than the surrounding mantle due to a 100-fold increase in the pre-exponential parameter of the mantle flow law ('100xIso weak'); and finally, *iv)* a fossil extensional/thrust mantle shear zone with strong olivine CPO surrounded by a mantle with equally strong CPO with [100]- and [010]-maximum orientations, respectively, parallel and normal to the imposed load ('Max. anisotropy dd'). Except for the latter case (i.e., black lines in Fig. 6), in which deformation developed for ~1 m.y., in all cases deformation developed for ~2.5 m.y. The models indicate that reactivation in extension results in faster thinning in the crust than in the mantle, whereas reactivation in compression results in faster thickening in the mantle (Fig. 6). Thinning rates are higher for the anisotropic cases and depend on the magnitude of the lateral strength contrasts, as indicated by the different slopes of the dashed lines. This dependence is non-linear with respect to CPO intensity. Fossil extensional/thrust mantle shear zones with strong (J = 12.7) or intermediate (J = 6.3) CPO intensities show comparable average vertical strains in both the crust and

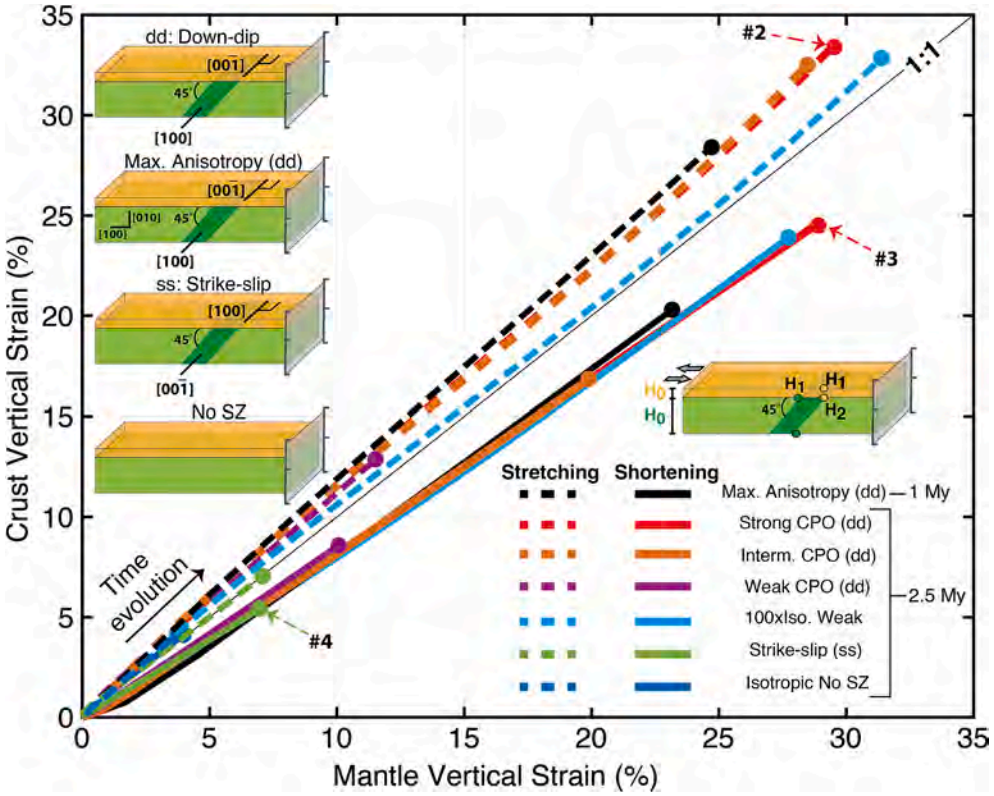

Fig. 6. Evolution over time of the average vertical strain, $\varepsilon_v\% = (\Delta H/H_0)$ x 100, in the mantle and crust estimated by dividing the change in thickness ($\Delta H = H_2 - H_1$) of the mantle and crust by their respective initial thickness (H_0), as in the cartoon atop the figure key. Simulations were run for shortening (continuous lines) or stretching (dashed lines) of a plate containing a mantle shear zone with extensional/thrust (down-dip: 'dd') past kinematic with different CPO intensities (strong J = 12.7 cases #2/3, intermediate J = 6.3, and weak J = 2.8), and with strike-slip ('ss') past kinematic with strong CPO intensity (case #4). Isotropic No SZ, 100xIso. Weak, and Max. Anisotropy (dd) are reference models, for details see text. All fossil mantle shear zones trend normal to the imposed load direction and dip by 45°. The orientation of the fossil mantle shear zones and associated olivine CPO is shown in the top left cartoons. The circles in the curves' end point indicate the average vertical strain achieved after ~2 m.y. of simulation, except for the black curve, which deformed for ~1 m.y.

the mantle. These vertical strains are a factor ~2.5 higher than those predicted for a similar mantle shear zone with weak CPO intensity (J = 2.8), and a factor ~5 to ~3.5 higher than those predicted for a homogenous isotropic lithosphere, and the dipping fossil strike-slip shear zones with strong CPO. Thickening rates are less dependent on past mantle kinematics and on the CPO intensity, as indicated by the similar slopes of the solid lines in Fig. 6. More details on the crustal deformation during reactivation of a fossil extensional/thrust mantle shear zone in extension (case #2) and compression (case #3) are presented in the supplementary Fig. S4.

4. Discussion

4.1. CPO-induced reactivation of fossil mantle shear zones and associated strain localization in the crust

The contrast in viscous anisotropy induced by a large-scale spatial variation in olivine CPO in the mantle affects the strain distribution in both the mantle and the crust. Viscous anisotropy may render a fossil mantle shear zone either weaker or stronger than its surroundings depending on the orientation of the new tectonic load relative to the olivine CPO (Figs. 1, 3, 4, 5). The strength contrast, and hence the magnitude of the strain localization, depends on both the orientation and intensity of the olivine CPO. Under conditions favoring mantle deformation by dislocation creep at high temperature and moderate pressure, as considered in the present models, the strength of a mantle volume decreases when the new tectonic load is oriented to favor glide in the easy [100]-direction in most olivine crystals composing the rock volume.

Within fossil extensional/thrust mantle shear zones, these conditions are optimally met for shear zones trending normal to the new tectonic load and dipping by 45° (Figs. 3, 4). This configuration leads to reactivation with maximum strain localization factors: strain rates in the mantle shear zone up to ~28 times higher than those in the isotropic surrounding mantle. In this case, strain localization in the mantle might triggers strain localization factor in the crust up to ~100. The magnitude of strain localization in the entire lithosphere depends on the strength contrast within the mantle. If the surrounding mantle has also a strong olivine CPO, but misoriented with respect to the active tectonic load, the lateral contrast in effective viscosity relative to the fossil mantle shear zone might be as high as three orders of magnitude (Supplementary Fig. S3). For similar orientations of the olivine CPO, the lateral strength contrast in the mantle depends on the CPO intensity. However, this dependence is non-linear, buffering for strong CPO, consistent with data for olivine aggregates deformed at high temperature at laboratory conditions (Hansen et al., 2012) and polycrystal plasticity simulations (Mameri et al., 2019). Hence, in general, the effect of varying CPO orientation on strain localization is more important than varying CPO intensity.

The range of loading-geometries producing reactivation of fossil extensional/thrust mantle shear zones, in both extension and compression, is greater than that leading to reactivation of fossil strike-slip mantle shear zones (Fig. 3). Furthermore, reactivating fossil extensional/thrust mantle shear zones in extension consistently leads to stronger strain localization than reactivating fossil strike-slip mantle shear zones or extensional/thrust shear zones in compression. CPO-induced viscous anisotropy associated with fossil extensional/thrust mantle shear zones has therefore a higher potential for producing reactivation compared to the fossil strike-slip ones, in particular when the lithosphere is subjected to extension. Indeed, in contrast to fossil vertical strike-slip mantle shear zones, fossil extensional/thrust mantle shear zones display markedly different behaviors when reactivated in compression or extension (Figs. 3, 4, 5). In extension, the maximum strain localization in the reactivated fossil extensional/thrust and strike-slip mantle shear zone is comparable, but the crust above the former exhibits significantly higher strain localization. In compression, maximum strain localization in both the mantle and crust is lower for reactivated extensional/thrust mantle shear zones compared to reactivated strike-slip mantle shear zones.

SO-VPSC simulations predict similar mechanical behaviors in

extension and compression for all loading-geometries (Fig. 1). This is consistent with the fact that, from the crystal deformation point of view, differences in mechanical behavior between compression and extension is only produced by twinning, which is not a possible deformation mechanism in olivine. In the geodynamical simulations, the mechanical behavior of reactivated fossil extensional/thrust mantle shear zones differ in extension and compression because of the distinct impact of gravity forces on the two deformation regimes. In extension, gravity forces add up to the tectonic forces (gravity acts parallel to the main stress σ_1), whereas in compression, gravity forces counteract the tectonic forces (gravity acts parallel to the minimum stress σ_3). Gravity also favors extensional deformation in the brittle crust. Lithospheric thinning results in lower average pressure at a given depth, which further reduces the brittle strength in the thinning domain right above the reactivated fossil extensional/thrust mantle shear zones. This favors strain localization in both the fossil mantle structure and in the newly formed crustal shear zones and faults. Conversely, lithospheric thickening results in higher average pressure, inhibiting strain localization in the brittle crust. In the simulations with a fossil vertical strike-slip mantle shear zone, the variations in lithospheric thickness across the simulation box are minor and gravity acts parallel to the intermediate stress σ_2, leading to similar behaviors in extension and compression.

4.2. *Implications for large-scale structural reactivation*

4.2.1. *The Pyrenees*

The Pyrenees orogen developed by inversion of an ancient rift formed in transtension along preexisting Variscan structures (Choukroune, 1992; Vissers and Meijer, 2012). Deep seismic refraction and receiver function profiles (ECORS-Pyrenees and ECORS-Arzacq)

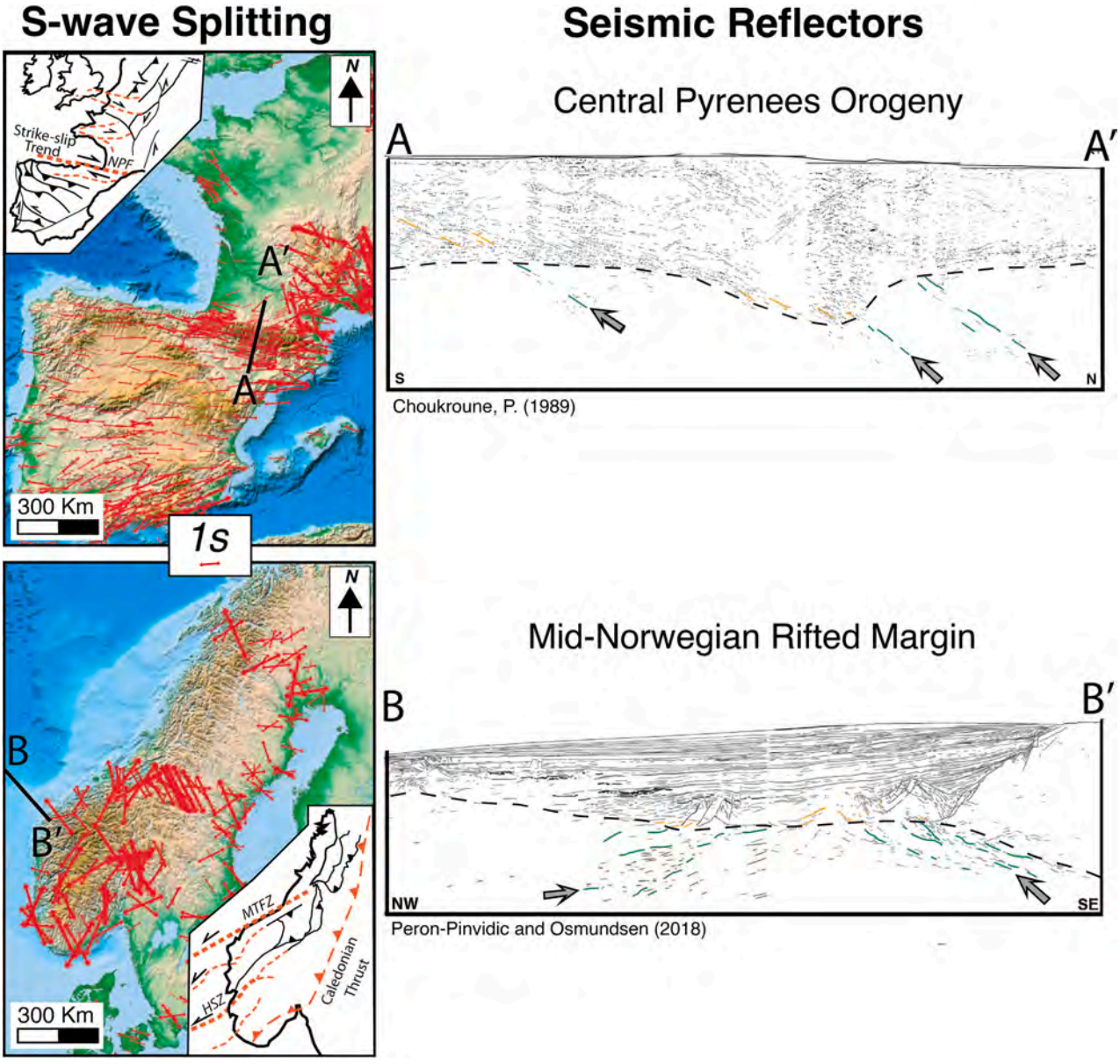

Fig. 7. Teleseismic shear-waves spliiting (left panel) depicted by red arrows oriented parallel to the fast polarization direction scaled by the magnitude of the delay time (from doi:10.18715/sks_splitting_database), deep seismic reflectors (right panel) mapped by the ECORS (Choukroune, 1989) and Møre crustal-scale transects (Peron-Pinvidic and Osmundsen, 2018) in the A) Pyrenees orogeny and B) Norwegian rifted margin, respectively. The dashed line on the profiles indicates the Moho. Grey arrows highlight kilometric-scale coherent dipping reflectors at mantle depths, which may represent large mantle shear zones; some continuous seismic reflectors in the crust and mantle were highlighted in orange and green, respectively. The trend of some major long-lived shear zones cited in the text is shown as dashed orange lines in the cartoons presented as inserts in the left panel. NPF: North Pyrenean Fault; MTFZ: Møre-Trøndelag Fault Zone; HSZ: Hardangerfjord Shear Zone.

indicate the presence of kilometric-scale planar structures with shallow to moderate dip angles extending to a depth of at least ~50 km in the lithospheric mantle (profile A-A' in Fig. 7a; Choukroune, 1989; Muñoz, 1992). Despite the past stretching and shortening history, polarization of fast teleseismic S-waves normal to the trend of the belt is not observed (Fig. 7a upper left). Fast teleseismic S-waves beneath the entire orogen show coherent polarization directions oriented sub-parallel to the trend of the belt (Bonnin et al., 2017). Fast propagation directions of Pn-waves, which sample the shallow lithospheric mantle, are also belt-parallel (Judenherc et al., 1999). These data suggest that olivine CPO in the lithospheric mantle beneath the Pyrenees records mainly belt-parallel displacements. They were interpreted as predominantly resulting from Variscan strike-slip deformation, with contribution from strike-slip deformation during the transtensional separation of Iberia from Eurasia and belt-parallel transport during Pyrenean collision (Vauchez and Nicolas, 1991; Vauchez et al., 1997; Barruol et al., 1998). Such a persistence of subparallel strike-slip motions over ~270 m.y. was previously proposed by Vauchez et al. (1997) as an indicator of CPO-induced structural reactivation.

Our previous analysis (Mameri et al., 2021), along with the present study, corroborates previous studies (Knoll et al., 2009; Tommasi et al., 2009) indicating that fossil vertical strike-slip mantle shear zones have a high potential for CPO-induced reactivation in response to an oblique tectonic load (case #1 in Fig. 3). The olivine-induced viscous anisotropy associated with the Variscan lithospheric-scale strike-slip shear zones was therefore likely a contributing factor to their reactivation during the early stages of the oblique rifting between Eurasia and Iberia, leading to transtension. This is consistent with the major component of strike-slip displacement in the initial stages of rifting in the Bay of Biscay in the western Pyrenees, inferred based on paleogeographic, magnetic and seismic data (Rosenbaum et al., 2002; Sibuet et al., 2004; Jammes et al., 2010). Paleomagnetic data also suggest that the early-stage of the convergence between Iberia and Eurasia in the future site of the Pyrenees was oblique to the major past strike-slip structures (Rosenbaum et al., 2002; Sibuet et al., 2004). Our models imply that even if the anisotropic fossil (Variscan) strike-slip shear zones were tilted or slightly rotated during the Pyrenean transtensional or the transpressional episodes, they could still be reactivated under an oblique load, which would result in significant along-strike displacement (Tommasi et al., 2009; Mameri et al., 2021). This interpretation is consistent with the Pyrenean belt-parallel displacement exceeding the belt-orthogonal displacement by factors 2–3 (Choukroune, 1992).

Along the Pyrenees, the fast teleseismic S-waves polarization rotates from azimuths ~80°-100° in the eastern and central domains of the belt to ~100°-120° in the western domain (Bonnin et al., 2017). Our geodynamic models predict that a variation of ~15° in the dip or trend of the fossil strike-slip shear zones may lead to a decrease in strain localization factor from ~30 to <2 and a >100-fold increase in effective viscosity. A more oblique CPO in the eastern domain could therefore have contributed to the observed variation in strain distribution along the belt (Chevrot et al., 2018), even in the case the major shear zone tilts moderately as suggested by the deep seismic profile (in Fig. 7a). However, in order to fully test this hypothesis, it is essential to include the evolution of anisotropic viscosity (Lev and Hager, 2008; Knoll et al., 2009; Király et al., 2020), which was not considered in our study.

4.2.2. The Norwegian margin

The Norwegian platform is a hyperextended margin developed onto former Caledonian orogenic structures (Fossen, 2010; Peron-Pinvidic and Osmundsen, 2018). Deep seismic profiles suggest the existence of shallowly dipping kilometric-scale planar structures in the lithospheric mantle (profile B-B′ in Fig. 7b; Peron-Pinvidic and Osmundsen, 2020). Fast polarization directions of teleseismic S-waves are bimodal, trending either NNW-SSE or ENE-WSW, respectively sub-parallel or oblique to the margin; both directions with high (>1 s) delay times (Fig. 7b bottom left; Grund and Ritter, 2020). The fast polarization of teleseismic S-waves parallel to the margin has been interpreted to be primarily associated with olivine CPO in Caledonian strike-slip mantle shear zones, while the fast polarization of teleseismic S-waves sub-perpendicular to oblique to the margin, and the dipping seismic reflectors, are interpreted as being associated with either the compressional Caledonian deformation or the subsequent extensional deformation during the Nord Atlantic rifting (Fossen et al., 2014; Grund and Ritter, 2020). The trend of these structures aligns with the fast polarization of teleseismic S-waves oriented along the Norwegian margin. This sub-parallelism between Paleozoic, Mesozoic, and Cenozoic lithospheric shear zones in the North Sea region suggests multiple reactivation episodes over ~300 m.y.

Extensional reactivation of major thrust shear zones was proposed to have impacted the post-orogenic collapse of the Caledonian belt (Fossen, 2000, 2010), which produced major extensional shear zones subparallel to the Caledonian belt, such as the Hardangerfjord shear zone (see HSZ in Fig. 7b bottom left). This shear zone, whose dip and trend directions roughly follow the NNW-SSE and ENE-WSW fast polarization directions of teleseismic S-waves, respectively, is associated nowadays with a major shallowly dipping structure that offsets vertically the Moho by ~10 km (Fossen et al., 2014). Reactivation of lithospheric detachment zones formed during the extensional collapse of the Caledonian belt, including the HSZ, was then suggested to have played an important role in shaping the west Norwegian margin (Phillips et al., 2019; Peron-Pinvidic and Osmundsen, 2020). The reactivation of the HSZ is proposed to have delineated basins and grabens in the southern Norwegian margin during the Nord Atlantic rifting (Doré et al., 1997; Phillips et al., 2019). These interpretations are corroborated by the present numerical models, which show that oblique extension applied to an anisotropic fossil thrust or extensional mantle shear zone is likely to produce strain localization in the lithosphere, notably in the crust.

Reactivation of Caledonian fossil strike-slip structures such as the Møre-Trøndelag Fault Zone (see MTFZ in Fig. 7b bottom left), a major steeply dipping structure trending sub-parallel to the ENE-WSW polarization direction of teleseismic S-waves, under a E-W extension direction has been interpreted to have accommodated differential stretching between basins opening during the early stages of the North Atlantic rift (Seranne, 1992; Doré et al., 1997; Braathen et al., 2002). The present models are in agreement with this view; a steeply dipping ENE-WSW trending strike-slip shear zones, such as the MTFZ, is highly prone to be reactivated under an oblique E-W extension.

Caledonian heterogeneities also impacted the subsequent development of rifts in the region (Fossen, 2000; Fossen et al., 2014; Peron-Pinvidic and Osmundsen, 2020), with olivine viscous anisotropy likely influencing this process. A shallowly dipping extensional shear zone, such as the HSZ, and a subvertical strike-slip shear zone with a similar trend, such as the MTFZ, have different potentials for CPO-induced reactivation during the oblique E-W Jurassic extension. The HSZ show low to moderate potential, and the MTFZ moderate to high. The relatively limited reactivation of the HSZ (Phillips et al., 2019) and the onshore oblique-slip displacement on the MTFZ (Doré et al., 1997) during this period are consistent with the reactivation potential predicted by the models. The regional extensional stress-field is inferred to have rotated to NW-SE in the subsequent phases of the Atlantic rifting (Doré et al., 1997, 1999), at higher angle to the trend of both structures. For such a loading-geometry, our models predict a factor ~2 higher strain rates in the isotropic mantle surrounding the vertical fossil strike-slip mantle shear zone. The poor orientation of the major strike-slip shear zones at that time might have led to strain delocalization, thereby facilitating the lateral migration of the North Atlantic rift (Lundin and Doré, 1997; Bell et al., 2014). In contrast, fossil extensional mantle shear zones would remain well-oriented for reactivation. The limited activity of the HSZ in the southern Norway region during the Early Cretaceous, despite its rather favorable orientation, would further point to lateral strain migration (Bell et al., 2014), for example towards extensional mantle shear zones with more moderate dip angles (e.g., 40°

to 50°), or to predominance of thermal-controlled reactivation in a more mature rift (Phillips et al., 2019).

5. Conclusion

Strain localization in the lithosphere resulting from lateral variations in olivine CPO within the mantle, associated with a fossil shear zone, was predicted using both polycrystal plasticity and geodynamical simulations. First, using the SO-VPSC model, the reactivation potential of shear zones characterized by typical olivine CPO formed under past shear-dominated extension/thrust or strike-slip kinematics was calculated as a function of the orientation of the CPO relative to the imposed load. Then, the reactivation potential of fossil mantle shear zones was further investigated using 3-D finite element geodynamical models with an CPO-induced anisotropic viscosity parameterized based on the polycrystal plasticity models. The mechanical response of a lithospheric plate containing a fossil anisotropic extensional/thrust or strike-slip mantle shear zone with a varied dip angle (between 30° and 90°) and trending normal to an extensional or compressive load was calculated and compared to the response of a fossil vertical strike-slip mantle shear zone trending at different angles to the tectonic load. Strain distribution, the magnitude of strain localization, lateral contrasts in effective viscosity, and also crust and lithospheric mantle thinning and thickening were quantified.

We observed that, for the relative strength of olivine slip systems representative of most of the continental lithospheric mantle, fossil mantle shear zones are likely to be reactivated if the tectonic load is oblique to the maximum concentration of [100] of the olivine CPO. The highest potential for reactivation of fossil strike-slip mantle shear zones occurs when the shear plane is vertical trending at 45° to the load direction. The highest potential for reactivation of fossil extensional or thrust mantle shear zones occurs when the fossil shear zone trends normal to the load direction and dips between 40° and 50°. Under extension, the maximum magnitude of strain localization in fossil strike-slip and extensional (or thrust) mantle shear zones is fairly similar, but strain localization in the crust atop the latter is much higher. Under compression, strain localization associated with reactivation of moderately dipping fossil extensional (or thrust) mantle shear zones is significantly lower than under extension, notably in the crust. This difference results from the action of gravity forces, which either add up (in extension) or counteract (in compression) the tectonic forces.

When olivine CPO in the fossil extensional (or thrust) mantle shear zone and surrounding mantle is strong and oriented to maximize their contrast in viscous anisotropy, the effective viscosity in the fossil shear zone can drop up to three orders of magnitude relative to the surroundings, and produce strain localization by up to two orders of magnitude in the lithosphere. If the surrounding mantle is isotropic, the maximum contrast in effective viscosity in the mantle decreases to two orders of magnitude, which can still induce significant strain localization: a factor ~30 in the mantle and ~100 in the crust. In general, strain localization associated with reactivation of fossil extensional/thrust mantle shear zones in a subsequent extensional event is higher than strain localization associated with reactivated fossil strike-slip mantle shear zones. In addition, the range of loading-geometries producing reactivation of fossil extensional/thrust mantle shear zones is larger than that of fossil strike-slip mantle shear zones.

The significant strength contrasts induced by spatial variation in olivine viscous anisotropy, together with the very long lifetimes of olivine CPO in the lithospheric mantle, may lead to the reactivation of fossil extension, thrust and strike-slip mantle shear zones in tectonic episodes spaced by hundreds of m.y. By examining the Norwegian margin and the Pyrenees large-scale structural inheritance, taking advantage of the abundant seismic anisotropy and profiling coverage, as well as their relatively well-known tectonic histories, we suggest that olivine viscous anisotropy triggered strain localization in major fossil extension, thrust and strike-slip mantle shear zones, notably in the early stages of the tectonic episodes. This contributed to shape their current lithospheric architecture. Long-lived lithospheric-scale shear zones exist in virtually every modern and ancient continental collision and rifting settings, calling for more studies on the effects of the associated viscous anisotropy in the mantle during large-scale tectonic inversions.

CRediT authorship contribution statement

Lucan Mameri: Conceptualization, Formal analysis, Investigation, Methodology, Validation, Visualization, Data curation, Writing - original draft, Writing - review & editing. **Andréa Tommasi:** Formal analysis, Funding acquisition, Project administration, Resources, Visualization, Supervision, Writing - original draft, Writing - review & editing. **Alain Vauchez:** Formal analysis, Supervision, Visualization. **Javier Signorelli:** Methodology, Software, Validation. **Riad Hassani:** Methodology, Software, Validation.

Declaration of Competing Interest

The authors declare that they have no known competing financial interests or personal relationships that could have appeared to influence the work reported in this paper.

Data availability

Codes and datasets from the present study are available upon request.

Acknowledgments

The authors thanks Ricardo Lebensohn and Carlos Tomé for making the VPSC7c code freely available. LM is grateful for Sonia Ouadahi's continuous encouragement. The authors acknowledge Samuel Angiboust (editor), Agnes Kiraly, and an anonymous reviewer for their valuable comments and suggestions, which were instrumental for improving our work. This project was funded by the European Union's Horizon 2020 research and innovation program under the Marie Sklodowska-Curie grant agreement ITN-CREEP (No. 642029).

Appendix A. Supplementary data

Supplementary data to this article can be found online at https://doi.org/10.1016/j.tecto.2023.229982.

References

Bai, Q., Mackwell, S.J., Kohlstedt, D.L., 1991. High-temperature creep of olivine single crystals 1. Mechanical results for buffered samples. J. Geophys. Res. Solid Earth 96 (B2), 2441–2463. https://doi.org/10.1029/90JB01723.

Barruol, G., Souriau, A., Vauchez, A., Diaz, J., Gallart, J., Tubia, J., Cuevas, J., 1998. Lithospheric anisotropy beneath the Pyrenees from shear wave splitting. J. Geophys. Res. Solid Earth 103 (B12), 30039–30053. https://doi.org/10.1029/98JB02790.

Bastow, I.D., Owens, T.J., Helffrich, G., Knapp, J.H., 2007. Spatial and temporal constraints on sources of seismic anisotropy: evidence from the Scottish Highlands. Geophys. Res. Lett. 34, L05305. https://doi.org/10.1029/2006gl028911.

Bell, R.E., Jackson, C.A.L., Whipp, P.S., Clements, B., 2014. Strain migration during multiphase extension: observations from the northern North Sea. Tectonics 33 (10), 1936–1963. https://doi.org/10.1002/2014TC003551.

Bonnin, M., Chevrot, S., Gaudot, I., Haugmard, M., PYROPE Working Group, 2017. Upper-mantle deformation beneath the Pyrenean domain inferred from SKS splitting in northern Spain and southern France. Geophys. J. Int. 210 (2), 898–910. https://doi.org/10.1093/gji/ggx193.

Bonnin, M., Tommasi, A., Hassani, R., Chevrot, S., Wookey, J., Barruol, G., 2012. Numerical modelling of the upper-mantle anisotropy beneath a migrating strike-slip plate boundary: the San Andreas Fault system. Geophys. J. Int. 191 (2), 436–458.doi. https://doi.org/10.1111/j.1365-246X.2012.05650.x.

Boudier, F., Coleman, R.G., 1981. Cross section through the peridotite in the Samail Ophiolite, Southeastern Oman Mountains. J. Geophys. Res. 86, 2573–2592. https://doi.org/10.1029/JB086iB04p02573.

Braathen, A., Osmundsen, P.T., Nordgulen, Ø., Roberts, D., Meyer, G.B., 2002. Orogen-parallel extension of the Caledonides in northern Central Norway: an overview. Nor. J. Geol./Nor. Geol. Foren. 82 (4).

Butler, R.W.H., 1989. The influence of pre-existing basin structure on thrust system evolution in the Western Alps. Geol. Soc. Lond., Spec. Publ. 44 (1), 105–122. https://doi.org/10.1144/GSL.SP.1989.044.01.07.

Catchings, R.D., Mooney, W.D., 1991. Basin and Range crustal and upper mantle structure, northwest to Central Nevada. J. Geophys. Res. Solid Earth 96 (B4), 6247–6267. https://doi.org/10.1029/91JB00194.

Chevrot, S., Sylvander, M., Diaz, J., Martin, R., Mouthereau, F., Manatschal, G., Masini, E., Calassou, S., Grimaud, F., Pauchet, H., Ruiz, M., 2018. The non-cylindrical crustal architecture of the Pyrenees. Sci. Rep. 8 (1), 1–8. https://doi.org/10.1038/s41598-018-27889-x.

Chopra, P.N., Paterson, A.M., 1981. The experimental deformation of dunite. Tectonophysics 78 (1–4), 453–473. https://doi.org/10.1016/0040-1951(81)90024-X.

Choukroune, P., 1989. The ECORS Pyrenean deep seismic profile reflection data and the overall structure of an orogenic belt. Tectonics 8 (1), 23–39. https://doi.org/10.1029/TC008i001p00023.

Choukroune, P., 1992. Tectonic evolution of the Pyrenees. Annu. Rev. Earth Planet. Sci. 20 (1), 143–158. https://doi.org/10.1146/annurev.ea.20.050192.001043.

Doré, A.G., Lundin, E.R., Fichler, C., Olesen, O., 1997. Patterns of basement structure and reactivation along the NE Atlantic margin. J. Geol. Soc. 154 (1), 85–92. https://doi.org/10.1144/gsjgs.154.1.0085.

Doré, A.G., Lundin, E.R., Jensen, L.N., Birkeland, Ø., Eliassen, P.E., Fichler, C., 1999. Principal tectonic events in the evolution of the northwest European Atlantic margin. In: Geological Society, London, Petroleum Geology Conference Series, vol. 5, No. 1. Geological Society of London, pp. 41–61. https://doi.org/10.1144/0050041. January.

Duclos, M., Savage, M.K., Tommasi, A., Gledhill, K.R., 2005. Mantle tectonics beneath New Zealand inferred from SKS splitting and petrophysics. Geophys. J. Int. 163 (2), 760–774. https://doi.org/10.1111/j.1365-246X.2005.02725.x.

Fossen, H., 2000. Extensional tectonics in the Caledonides: synorogenic or postorogenic? Tectonics 19 (2), 213–224. https://doi.org/10.1029/1999TC900066.

Fossen, H., 2010. Extensional tectonics in the North Atlantic Caledonides: a regional view. Geol. Soc. Lond., Spec. Publ. 335 (1), 767–793. https://doi.org/10.1144/SP335.31.

Fossen, H., Gabrielsen, R.H., Faleide, J.I., Hurich, C.A., 2014. Crustal stretching in the Scandinavian Caledonides as revealed by deep seismic data. Geology 42 (9), 791–794. https://doi.org/10.1130/G35842.1.

Frets, E.C., Tommasi, A., Garrido, C.J., Vauchez, A., Mainprice, D., Targuisti, K., Amri, I., 2014. The Beni Bousera peridotite (Rif Belt, Morocco): an oblique-slip low-angle shear zone thinning the subcontinental mantle lithosphere. J. Petrol. 55 (2), 283–313. https://doi.org/10.1093/petrology/egt067.

Gouriet, K., Cordier, P., Garel, F., Thoraval, C., Demouchy, S., Tommasi, A., Carrez, P., 2019. Dislocation dynamics modelling of the power-law breakdown in olivine single crystals: toward a unified creep law for the upper mantle. Earth Planet. Sci. Lett. 506, 282–291. https://doi.org/10.1016/j.epsl.2018.10.049.

Grund, M., Ritter, J.R., 2020. Shear-wave splitting beneath Fennoscandia—evidence for dipping structures and laterally varying multilayer anisotropy. Geophys. J. Int. 223 (3), 1525–1547. https://doi.org/10.1093/gji/ggaa388.

Hansen, L.N., Zimmerman, M.E., Kohlstedt, D.L., 2012. Laboratory measurements of the viscous anisotropy of olivine aggregates. Nature 492 (7429), 415–418. https://doi.org/10.1038/nature11671.

Hartog, R., Schwartz, S.Y., 2001. Depth-dependent mantle anisotropy below the San Andreas fault system: Apparent splitting parameters and waveforms. J. Geophys. Res. Solid Earth 106 (B3), 4155–4167. https://doi.org/10.1029/2000JB900382.

Hassani, R., Jongmans, D., Chry, J., 1997. Study of plate deformation and stress in subduction processes using two-dimensional numerical models. J. Geophys. Res. Solid Earth 102 (B8). https://doi.org/10.1029/97JB01354, 17,95117,965.

Hill, R., 1948. A theory of the yielding and plastic flow of anisotropic metals. Proc. Royal Soc. Lond. Ser. A Math. Phys. Sci. 193 (1033), 281–297. https://doi.org/10.1098/rspa.1948.0045. May 27.

Hirn, A., Jiang, M., Sapin, M., Diaz, J., Nercessian, A., Lu, Q.T., Gallart, J., 1995. Seismic anisotropy as an indicator of mantle flow beneath the Himalayas and Tibet. Nature 375 (6532), 571–574. https://doi.org/10.1038/375571a0.

Jackson, J.A., 1980. Reactivation of basement faults and crustal shortening in orogenic belts. Nature 283 (5745), 343–346. https://doi.org/10.1038/283343a0.

Jammes, S., Tiberi, C., Manatschal, G., 2010. 3D architecture of a complex transcurrent rift system: the example of the Bay of Biscay–Western Pyrenees. Tectonophysics 489 (1–4), 210–226. https://doi.org/10.1016/j.tecto.2010.04.023.

Judenherc, S., Granet, M., Boumbar, N., 1999. Two- dimensional anisotropic tomography of lithosphere beneath France using regional arrival times. J. Geophys. Res. 104, 13201–13215. https://doi.org/10.1029/1999JB900079.

Kaczmarek, M.A., Tommasi, A., 2011. Anatomy of an extensional shear zone in the mantle, Lanzo massif, Italy. Geochem. Geophys. Geosyst. 12 (8) https://doi.org/10.1029/2011GC003627.

Király, Á., Conrad, C.P., Hansen, L.N., 2020. Evolving viscous anisotropy in the upper mantle and its geodynamic implications. Geochem. Geophys. Geosyst. 21 (10) https://doi.org/10.1029/2020GC009159 e2020GC009159.

Knoll, M., Tommasi, A., Logé, R.E., Signorelli, J.W., 2009. A multiscale approach to model the anisotropic deformation of lithospheric plates. Geochem. Geophys. Geosyst. 10 (8) https://doi.org/10.1029/2009GC002423.

Lev, E., Hager, B.H., 2008. Prediction of anisotropy from flow models: a comparison of three methods. Geochem. Geophys. Geosyst. 9 (7) https://doi.org/10.1029/2008GC002032.

Lundin, E.R., Doré, A.G., 1997. A tectonic model for the Norwegian passive margin with implications for the NE Atlantic: Early Cretaceous to break-up. J. Geol. Soc. 154 (3), 545–550. https://doi.org/10.1144/gsjgs.154.3.0545.

Mameri, L., Tommasi, A., Signorelli, J., Hansen, L.N., 2019. Predicting viscoplastic anisotropy in the upper mantle: a comparison between experiments and polycrystal plasticity models. Phys. Earth Planet. Inter. 286, 69–80. https://doi.org/10.1016/j.pepi.2018.11.002.

Mameri, L., Tommasi, A., Signorelli, J., Hassani, R., 2021. Olivine-induced viscous anisotropy in fossil strike-slip mantle shear zones and associated strain localization in the crust. Geophys. J. Int. 224 (1), 608–625. https://doi.org/10.1093/gji/ggaa400.

Meyers, C.D., Kohlstedt, D.L., 2021. Experimental measurements of anisotropic viscosity in naturally sourced dunite with a preexisting CPO. Tectonophysics 815, 228949. https://doi.org/10.1016/j.tecto.2021.228949.

Muñoz, J.A., 1992. Evolution of a continental collision belt: ECORS-Pyrenees crustal balanced cross-section. In: Thrust Tectonics. Springer, Dordrecht, pp. 235–246. https://doi.org/10.1007/978-94-011-3066-0_21.

Nicolas, A., Christensen, N.I., 1987. Formation of anisotropy in upper mantle peridotites-a review. Compos. Struct. Dynamics Lithosphere-Asthenosphere Syst. 16, 111–123. https://doi.org/10.1029/GD016p0111.

Nicolas, A., Hirn, A., Nicolich, R., Polino, R., 1990. Lithospheric wedging in the western Alps inferred from the ECORS-CROP traverse. Geology 18 (7), 587–590. https://doi.org/10.1130/0091-7613(1990)018<0587:LWITWA>2.3.CO;2.

Paterson, M.S., Luan, F.C., 1990. Quartzite rheology under geological conditions. Geol. Soc. Lond., Spec. Publ. 54 (1), 299–307. https://doi.org/10.1144/GSL.SP.1990.054.01.26.

Peron-Pinvidic, G., Osmundsen, P.T., 2018. The Mid Norwegian-NE Greenland conjugate margins: rifting evolution, margin segmentation, and breakup. Mar. Pet. Geol. 98, 162–184. https://doi.org/10.1016/j.marpetgeo.2018.08.011.

Peron-Pinvidic, G., Osmundsen, P.T., 2020. From orogeny to rifting: insights from the Norwegian 'reactivation phase'. Sci. Rep. 10 (1), 1–8. https://doi.org/10.1038/s41598-020-71893-z.

Phillips, T.B., Fazlikhani, H., Gawthorpe, R.L., Fossen, H., Jackson, C.A., Bell, R.E., Faleide, J.I., Rotevatn, A., 2019. The influence of structural inheritance and multiphase extension on rift development, the NorthernNorth Sea. Tectonics. 38 (12), 4099–4126. https://doi.org/10.1029/2019TC005756. Dec.

Ponte Castañeda, P., 2002. Second-order homogenization estimates for nonlinear composites incorporating field fluctuations: I-theory. J. Mech. Phys. Solids 50 (4), 737–757. https://doi.org/10.1016/S0022-5096(01)00099-0.

Rosenbaum, G., Lister, G.S., Duboz, C., 2002. Relative motions of Africa, Iberia and Europe during Alpine orogeny. Tectonophysics 359 (1–2), 117–129. https://doi.org/10.1016/S0040-1951(02)00442-0.

Saspiturry, N., Allanic, C., Razin, P., Issautier, B., Baudin, T., Lasseur, E., Leleu, S., 2020. Closure of a hyperextended system in an orogenic lithospheric pop-up, Western Pyrenees: the role of mantle buttressing and rift structural inheritance. Terra Nova. https://doi.org/10.1111/ter.12457.

Sénéchal, G., Rondenay, S., Mareschal, M., Guilbert, J., Poupinet, G., 1996. Seismic and electrical anisotropies in the lithosphere across the Grenville Front, Canada. Geophys. Res. Lett. 23 (17), 2255–2258. https://doi.org/10.1029/96GL01410.

Seranne, M., 1992. Late Palaeozoic kinematics of the Møre-Trøndelag Fault Zone and adjacent areas, Central Norway. Nor. Geol. Tidsskr. 72, 141–158.

Sibuet, J.C., Srivastava, S.P., Spakman, W., 2004. Pyrenean orogeny and plate kinematics. J. Geophys. Res. Solid Earth 109 (B8). https://doi.org/10.1029/2003JB002514.

Signorelli, J., Tommasi, A., Hassani, R., Mameri, L., 2021. An effective parameterization of texture-induced viscous anisotropy in orthotropic materials with application for modeling geodynamical flows. J. Theor. Comput. Appl. Mech. https://doi.org/10.46298/jtcam.6737.

Tommasi, A., Vauchez, A., 2001. Continental rifting parallel to ancient collisional belts: an effect of the mechanical anisotropy of the lithospheric mantle. Earth Planet. Sci. Lett. 185 (1–2), 199–210. https://doi.org/10.1016/S0012-821X(00)00350-2.

Tommasi, A., Vauchez, A., 2015. Heterogeneity and anisotropy in the lithospheric mantle. Tectonophysics 661, 11–37. https://doi.org/10.1016/j.tecto.2015.07.026.

Tommasi, A., Tikoff, B., Vauchez, A., 1999. Upper mantle tectonics: three-dimensional deformation, olivine crystallographic fabrics and seismic properties. Earth Planet. Sci. Lett. 168 (1–2), 173–186. https://doi.org/10.1016/S0012-821X(99)00046-1.

Tommasi, A., Knoll, M., Vauchez, A., Signorelli, J.W., Thoraval, C., Logé, R., 2009. Structural reactivation in plate tectonics controlled by olivine crystal anisotropy. Nat. Geosci. 2 (6), 423–427. https://doi.org/10.1038/ngeo528.

Vauchez, A., Nicolas, A., 1991. Mountain building: strike-parallel displacements and mantle anisotropy. Tectonophysics 185, 183–201. https://doi.org/10.1016/0040-1951(91)90443-V.

Vauchez, A., Tommasi, A., 2003. Wrench faults down to the asthenosphere: geological and geophysical evidence and thermomechanical effects. Geol. Soc. Lond., Spec. Publ. 210 (1), 15–34. https://doi.org/10.1144/GSL.SP.2003.210.01.02.

Vauchez, A., Barruol, G., Tommasi, A., 1997. Why do continents break-up parallel to ancient orogenic belts? Terra Nova 9 (2), 62–66. https://doi.org/10.1111/j.1365-3121.1997.tb00003.x.

Vissers, R.L.M., Meijer, P.T., 2012. Iberian plate kinematics and Alpine collision in the Pyrenees. Earth Sci. Rev. 114 (1–2), 61–83. https://doi.org/10.1016/j.earscirev.2012.05.001.

Vauchez, A., Tommasi, A., Mainprice, D., 2012. Faults (shear zones) in the Earth's mantle. Tectonophysics 558, 1–27. https://doi.org/10.1016/j.tecto.2012.06.006.

Vissers, R.L.M., Drury, M.R., Hoogerduijn, E.H., Spiers, C.J., Van der Wal, D., 1995. Mantle shear zones and their effect on lithosphere strength during continental breakup. Tectonophysics 249 (3–4), 155–171. https://doi.org/10.1016/0040-1951(95)00033-J.

Wilson, J.T., 1966. Did the Atlantic Close and then Re-Open? Nature 211, 676–681. https://doi.org/10.1038/211676a0.